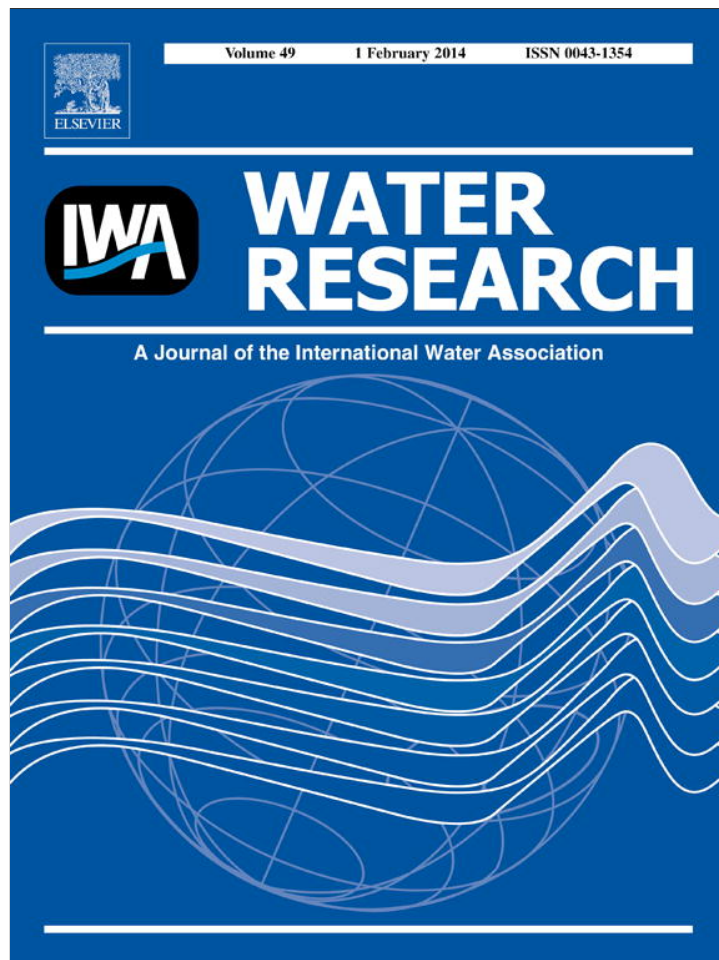


Provided for non-commercial research and education use.  
Not for reproduction, distribution or commercial use.



This article appeared in a journal published by Elsevier. The attached copy is furnished to the author for internal non-commercial research and education use, including for instruction at the authors institution and sharing with colleagues.

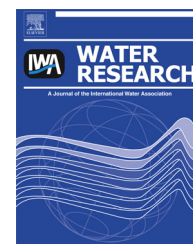
Other uses, including reproduction and distribution, or selling or licensing copies, or posting to personal, institutional or third party websites are prohibited.

In most cases authors are permitted to post their version of the article (e.g. in Word or Tex form) to their personal website or institutional repository. Authors requiring further information regarding Elsevier's archiving and manuscript policies are encouraged to visit:

<http://www.elsevier.com/authorsrights>

Available online at [www.sciencedirect.com](http://www.sciencedirect.com)

ScienceDirect

journal homepage: [www.elsevier.com/locate/watres](http://www.elsevier.com/locate/watres)

# Permeability and selectivity of reverse osmosis membranes: Correlation to swelling revisited

Emil Dražević<sup>a,\*</sup>, Krešimir Košutić<sup>a</sup>, Viatcheslav Freger<sup>b,\*\*</sup>

<sup>a</sup> University of Zagreb, Faculty of Chemical Engineering and Technology, Marulićev trg 19, 10000 Zagreb, Croatia

<sup>b</sup> Technion – Israel Institute of Technology, Wolfson Department of Chemical Engineering, Technion City, 32000 Haifa, Israel

## ARTICLE INFO

### Article history:

Received 17 July 2013

Received in revised form

9 October 2013

Accepted 11 October 2013

Available online 20 October 2013

### Keywords:

Reverse osmosis

Nanofiltration

Permeability

Swelling

Salt rejection

Dielectric exclusion

## ABSTRACT

Membrane swelling governs both rejection of solutes and permeability of polymeric membranes, however very few data have been available on swelling in water of salt-rejecting reverse osmosis (RO) membranes. This study assesses swelling, thickness and their relation to water permeability for four commercial polyamide (PA) RO membranes (SWC4+, ESPA1, XLE and BW30) using atomic force microscopy (AFM) and attenuated total reflection Fourier transform IR spectroscopy (ATR-FTIR). ATR-FTIR offered a significantly improved estimate of the actual barrier thickness of PA, given AFM is biased by porosity (“fluffy parts”) or wiggling of the active layer or presence of a coating layer. Thus obtained intrinsic permeability (permeability times thickness) and selectivity of aromatic polyamides plotted versus swelling falls well on a general trend, along with previously reported data on several common materials showing RO and NF selectivity. The observed general trend may be rationalized by viewing the polymers as a random composite medium containing molecularly small pores. The results suggest that the combination of a rigid low dielectric matrix, limiting the pore size, with multiple hydrophilic H-bonding sites may be a common feature of RO/NF membranes, allowing both high permeability and selectivity.

Crown Copyright © 2013 Published by Elsevier Ltd. All rights reserved.

## 1. Introduction

The swelling of polymeric membranes is an important parameter that may affect their physical structure and affinity to solvents and solutes and thus their permeability and rejection of solutes (Tarleton et al., 2006). It is a complex phenomenon that depends on the affinity between the solvent and the polymer, presence of osmotically active species (e.g., mobile counter ions) and degree of cross-linking of the polymer. Swelling of polymeric membranes in water, i.e., their equilibrium water content is of particular interest for the processes of reverse osmosis (RO) and nanofiltration (NF)

widely used in the desalination and water purification. In this context, fully aromatic polyamide and semi-aromatic poly(piperazine amide) (Petersen, 1993) are most common polymers used to make the rejecting layers of commercial RO/NF membranes. Commercial RO/NF polyamide-based membranes can be defined as dense polymer structures with free void spaces through which transport of water occurs under a pressure gradient. Previous studies showed that these polyamide materials membranes may largely vary in terms of swelling as well as thickness (Coronell et al., 2011) and structural heterogeneity and morphology (Freger, 2003). In addition, they may contain several types of nanopores (Kim

\* Corresponding author.

\*\* Corresponding author.

E-mail addresses: [edraz@fkit.hr](mailto:edraz@fkit.hr) (E. Dražević), [vfregertx@technion.ac.il](mailto:vfregertx@technion.ac.il) (V. Freger).

et al., 2005; Košutić et al., 2000), which may affect their water uptake and formation of paths along which water moves across the membrane under a pressure gradient (Meares, 1976). The nanopores could be of various shapes, open or closed, and may or may not form a continuous network. Very little is known of membrane water uptake and is there a correlation between water content and water permeability and, likely, rejection of solutes. For instance, Freger reported that swelling of low flux RO membranes is in general lower compared to swelling of high flux NF membranes due their rigid aromatic structure and high degree of cross-linking (Freger, 2004), which may be related to higher rejection of solutes achieved by RO membranes compared to NF. Recent data by Lee et al. indicate that polyamide nanoporous structure undergoes little pore swelling upon water uptake (Lee et al., 2013), which confirms the high rigidity of this material leading to low swelling.

In 1977 Meares carried out a systematic study (Meares, 1977), in which he measured water content (swelling) and intrinsic water permeability (i.e., permeability normalized to thickness) of homogeneous films of cellulose acetate cast from different solvents and some other polymers. His results fall remarkably well on a single trend of intrinsic permeability versus water content, on which some polyamide membranes fall as well (Freger, 2004). However, some polyamide membranes noticeably deviated from this trend, which was explained by the incorrect estimates of the thickness of the polyamide layer (Freger, 2004). The aim of this study is to find a proper way to address this problem for several polyamide composite membranes and locate them on the general trend.

Compared to macroscopic films, e.g., the cellulose acetate films used by Meares, the water content (swelling) of polyamide-based membranes is difficult to measure directly because of very small thickness ( $\sim 100$  nm) and mass ( $\sim 10$   $\mu\text{g}/\text{cm}^2$ ) of the selective polyamide layer (Coronell et al., 2011). In this study, a method developed earlier and based on atomic force microscopy (AFM) (Freger, 2004) is used to evaluate swelling by measuring thicknesses of dry and wet films taken from different RO/NF membranes. However, AFM cannot correctly evaluate true thickness and swelling of some RO membranes (Freger, 2003). For instance, it is difficult for high-flux membranes that have a “sandwich structure” where the thin active core layer is hidden within a much thicker layer of loose porous polyamide (Freger, 2003, 2004) or coated membranes (Tang et al., 2007). In this study swelling measurements by AFM are combined with estimates by ATR-FTIR to obtain more consistent estimates of thickness for all types of polyamide membranes, more accurately estimate their intrinsic permeability and thus re-examine and discuss the correlation of water permeability through dense polymeric materials with swelling.

## 2. Materials and methods

### 2.1. Membranes and materials

Four commercial membranes were examined in this study: a high water flux membranes XLE (Dow/Filmtec™, Midland, MI, USA) and ESPA1 (Hydranautics/Nitto Denko, Oceanside, CA, USA), a sea water membrane SWC4+ (Hydranautics/Nitto

Denko, Oceanside, CA, USA) and a brackish water membrane BW30 (Dow/Filmtec™, Midland, MI, USA). Technical specifications of the membranes are found in Table 1. Membranes were kindly supplied by manufacturers as flat sheet samples and stored in dry state before use.

### 2.2. Isolation of the PA layer

The method of isolation of membrane's selective layer is described elsewhere (Freger, 2004). Briefly, the non-woven fabric was carefully peeled off the membrane to leave only the polysulfone (PSU) and PA layers. Afterwards the membrane was gently attached (PA side facing down to the surface) with a drop of toluene which softens both PA and PSU layer. Once dried film adhered to the surface by capillary forces, PSU was gently washed away with N, N-dimethyl formamide until all PSU was removed. In this way free-standing PA films were prepared on silicon wafers for the AFM measurements or on the diamond crystal of an ATR setup for the FTIR-ATR measurements.

### 2.3. FTIR-ATR measurements

The spectra of PA films were recorded in the mid IR range ( $400\text{--}4000$   $\text{cm}^{-1}$ ) on a Bruker Vertex 70 series FTIR spectrometer equipped with a Bruker Platinum ATR accessory with a single reflection diamond crystal ( $n = 2.4$ ). Infrared (IR) spectra were recorded at  $4$   $\text{cm}^{-1}$  resolution and 24 scans. PA films of all membranes were isolated and attached directly to the ATR crystal, while the background of a bare crystal was recorded just before deposition of the film.

### 2.4. Atomic force microscopy

The thickness and swelling of PA layers were measured using AFM. The method is described in details elsewhere (Freger, 2004). Samples were imaged using a Bruker Innova AFM microscope at room temperature ( $\sim 25^\circ$  C). Bruker SNL cantilevers (triangular D) with nominal spring constant  $0.06$  N/m were used in contact mode and mounted on an APMC-0001 Microcell for liquid imaging with small amount of liquid ( $50\text{--}100$   $\mu\text{l}$ ). PA films isolated on Si wafer were gently scratched using a sharp needle to form very narrow strips of PA surrounded on both sides by a bare Si surface. Strips were first imaged in dry state, then covered with deionized water, allowed 30 min to equilibrate, and then imaged again in exactly the same place as in the dry state. The images were flattened using Bruker NanoScope Analysis software using

**Table 1 – Characteristics of the membranes tested.**

	XLE	ESPA1	BW30	SWC4+
Selective layer material	PA	PA	PA	PA
$L_p$ , ( $\text{L m}^{-2} \text{h}^{-1} \text{bar}^{-1}$ ) <sup>a</sup>	7.4	5.4	3.0	0.7
Rejection of NaCl, $f_{\text{NaCl}}$	0.995 <sup>b</sup>	0.994 <sup>b</sup>	0.995 <sup>b</sup>	0.998 <sup>c</sup>

<sup>a</sup> Measured with deionized water at  $25^\circ$  C.  
<sup>b</sup> Manufacturers data: 2000 ppm NaCl at 15% recovery, pressure 0.86 MPa.  
<sup>c</sup> Manufacturers data: 2000 ppm NaCl, 10% recovery, pressure 5.5 MPa.

first and second order flattening routines that were applied only to the bare Si on both sides of the PA strip. The average thickness of the PA strip, both in dry and wet state, was determined as the distance between maxima of the two highest peaks in depth histograms corresponding to bare Si and film-covered wafer. Water content (swelling) on the wet basis in the films was then calculated from the average of three independent measurements using the formula

$$\Phi = (d_{\text{AFM wet}} - d_{\text{AFM dry}}) / d_{\text{AFM wet}} \quad (1)$$

### 2.5. RO/NF experimental setup and analysis

Experimental setup is described elsewhere (Dražević et al., 2012). Briefly, RO tests were carried out in a Sterlitech SEPA II cross-flow cell of membrane area 0.0138 m<sup>2</sup> and channel dimensions 14.5 × 9.5 × 0.17 cm<sup>3</sup> (length × width × height). The recovery rate was very low, about 1–3%. Milipore deionized water was circulated through the cell at fluid velocity of 0.42 m s<sup>-1</sup>. Temperature was held constant at 25.0 ± 0.1 °C.

The salt permeability of the membranes was measured using 35,000 ppm NaCl solution, at 25.0 ± 0.1 °C and cross-flow velocity of 0.42 m s<sup>-1</sup>. In these experiments the volume flux,  $J_v$ , was kept constant at 2.5 μm s<sup>-1</sup> for all membranes by adjusting the pressure. The rejection  $R$  was determined by measuring the conductivity of the feed and permeate. The salt permeability coefficient  $B$  was calculated from the volume flux  $J_v$  and rejection using the following equation

$$B = J_v \frac{1 - R}{R} \quad (2)$$

## 3. Results and discussion

### 3.1. AFM measurements

One typical flattened image of a narrow strip of SWC4+ and its corresponding height histograms in dry state and in water are

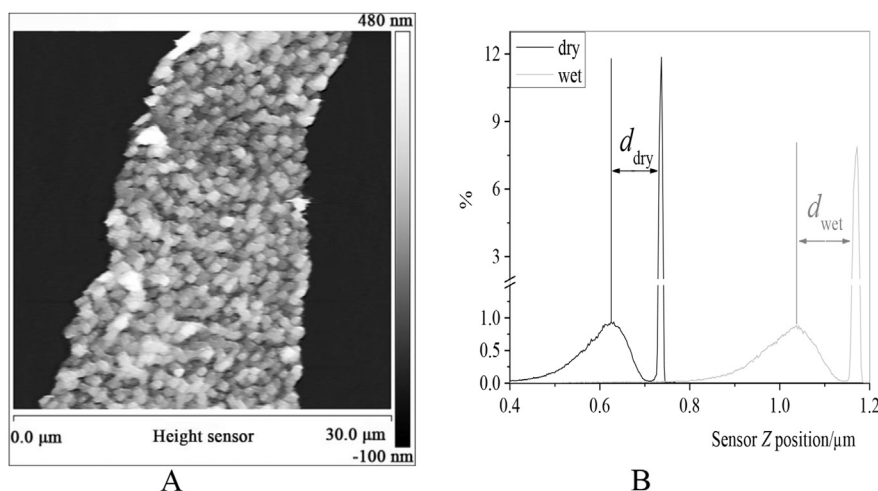


**Fig. 1** – (A) A typical flattened topographic image of a one-layer polyamide strip isolated from a SWC4+ membrane on a Si wafer. (B) Typical histograms obtained for dry and wet SWC4+ film sample yielding a dry thickness 112 nm, wet thickness 129 nm, and  $\Phi = 0.13$ .

presented in Fig. 1. Table 2 summarizes thickness of dry and wet films for different membrane samples determined at exactly the same location in air and under water and corresponding swelling degrees deduced from the histograms using Eq. (1). Table 2 shows swelling of the four membranes calculated as an average of three such independent measurements (i.e., for 3 different locations) on particular narrow film strips ( $\Phi_{\text{av}} = (\Phi_1 + \Phi_2 + \Phi_3)/3$ ).

Tables 1 and 2 show that the membranes involved show significant, an order of magnitude, differences in pure water permeability ( $L_p$ ) and swelling, not necessarily correlated with each other if thickness is not taken into consideration. The most permeable XLE membrane showed the highest swelling of 53% (on the wet basis) (Table 2), yet only slightly less permeable ESPA1, for which AFM also yields a similar thickness, showed only 7% swelling. Freger (2003, 2004) reported that ESPA1 membrane has an open and porous (“fluffy”) structure at the surface with a dense and thin core layer buried within the “fluff”. TEM images in Freger’s study (Freger, 2003) indicate that the true thickness of ESPA layer is probably about 10–15% of thickness that AFM measures. Yet, TEM images of SWC1 membrane (analogous to SWC4+ used here) showed a much more homogeneous structure with a small fraction of voids. It should be noted that porous “fluffy” parts on the surface could interfere with swelling measurement of ESPA1 membranes and introduce some error. However, the low swelling of this membrane suggests that the “fluffy” parts of ESPA1 are apparently built of the same rigid polymer as the dense core, thus its measured swelling is of the same order and, actually, even less than for the densest SWC4+ membrane.

Conversely, the high swelling of XLE indicates the polyamide is significantly less rigid. It then appears that the high permeability of the two high-flux membranes, XLE and ESPA1, is achieved in different ways, namely, through a looser and more swollen polymer for the former and a very thin dense core, i.e., smaller thickness, for the latter. Interestingly, BW30 shows a very different swelling from the other RO

**Table 2 – Thickness of dry ( $d_{AFM\ dry}$ ) and wet ( $d_{AFM\ wet}$ ) films and corresponding water contents ( $\phi$ ) of membranes tested.**

Membrane	$d_{AFM\ dry}$	Err $d_{AFM\ dry}$	$d_{AFM\ wet}$	Err $d_{AFM\ wet}$	$\phi$	Err $\phi^a$
XLE	179.3	24.4	273.7	28.2	0.35	0.02
ESPA	190.2	50.1	203.5	57.5	0.07	0.02
BW30	121.7	7.8	152	10.7	0.19	0.08
SWC4+	122	29	139.3	24.9	0.13	0.06

<sup>a</sup>  $err\ \phi = \sqrt{\frac{1}{N} \sum_{i=1}^N (\phi(i) - \phi)^2}$  where  $\phi = \frac{1}{N} \sum_{i=1}^N \phi(i)$ .

membranes, as high as 26%. The exact chemistry of BW30 is not reported by the manufacturer, but X-ray photoelectron spectroscopy (XPS) analysis shows a high oxygen content and very low nitrogen content (see next section), which suggests that this membrane is coated with another hydrophilic material (Tang et al., 2009, 2007). Coating is likely to increase its measured swelling and AFM thickness, so that the true thickness of BW30, beneath the coating, was re-evaluated using FTIR-ATR measurements together with that of ESPA1 and XLE in the following section.

### 3.2. Evaluation of spectroscopic thickness of membranes – FTIR

ATR-FTIR spectra (Fig. 2) of the active layer isolated from SWC4+, ESPA and XLE membranes show that their chemistry is virtually identical, meaning their rejecting layers can be viewed as having a similar chemistry, even though they have different properties in terms of salt rejection and water permeability (Table 2). The similarity between SWC4, XLE and ESPA membranes is also indicated by their atomic compositions analysed using XPS. Tang et al. (Tang et al., 2007) found the O/N ratio for SWC4, XLE and ESPA3 is fairly similar, 1.2, 1.0 and 1.0, respectively. Oxygen content of these membranes was about the same (13%), while nitrogen content of SWC4 (11%) was only slightly lower compared to XLE and ESPA3 (13%). These results are consistent with polyamide chemistry.

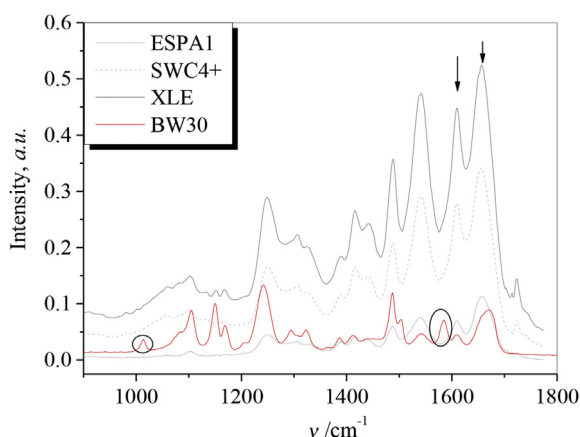


**Fig. 2 – IR spectra of one layer of SWC4+, XLE, BW30 and ESPA1 directly isolated on ATR diamond. The circled bands in the spectrum of BW30 apparently belong to the coating layer.**

In contrast, XPS of BW30 showed a different surface chemistry with significantly increased oxygen content (29%) and reduced nitrogen content (only 3%) (Tang et al., 2009). IR spectra in Fig. 2 show that the active layer isolated from BW30 contain the same bands as SWC4+, XLE and ESPA1, yet there are also distinct bands assignable to polymeric alcohol coating (Tang et al., 2007).

It may be noted, however, that the intensity of the polyamide bands, which linearly correlates with the total amount of polymer per unit area for films of submicron thickness, is different for all membranes. It is then proposed here to use ATR-FTIR intensity of appropriate bands of polyamide as a more adequate measure of the polyamide thickness. Thus, for BW30 this estimate would not be affected by the coating and for ESPA1 highly porous “fluff” would contribute much less to ATR-FTIR than it does to AFM. To convert ATR-FTIR intensity to thickness, one may take advantage of the fact that SWC4+ membrane appears to have no “fluff” in TEM, thus the ratio of an ATR-FTIR band of polyamide to AFM thickness of this membrane approximately corresponds to 100% polyamide. Then the volume fraction of polyamide in the active layer of XLE, BW30 and ESPA1 may be determined as the ratio of the intensity of this band to AFM thickness of the dry film normalized to the same ratio for SWC4+. To improve accuracy and reproducibility of the measurements stacks of up to five films were isolated from the same membrane. Fig. 3A plots the thickness of such dry stacks determined by AFM and Fig. 3B does it for the areas,  $Y$ , of 1609 and 1650  $\text{cm}^{-1}$  bands in ATR-FTIR spectra (see Fig. 3C) versus the number of stacked layers,  $N$ . Both plots show a good linear correlation with the number of layers, suggesting that all layers in the stack have a similar thickness and the slope yields the average intensity per layer. Stacks of XLE, BW30 and ESPA1 membranes yield similar linear plots but the ratio of the slope obtained from ATR-FTIR to that by AFM is significantly smaller (Table 3.) than for SWC4+ (cf. corresponding IR bands in Fig. 3D). Obviously, the ratio of the ATR-FTIR-based and AFM-based slopes is proportional to the volume fraction of polymer in these membranes and this fraction is evaluated assuming that it is 100% for SWC4+. The product of this volume fraction and the AFM thickness yields the corrected thickness, equivalent to that of polyamide collapsed to a dense film. This thickness referred to below as the “spectroscopic thickness”. Thus determined polymer volume fractions and dry spectroscopic thickness  $d_s$  are summarized in Table 3.

A fairly high polymer volume fraction of 0.8 obtained for XLE (Table 3) along with a high swelling of this membrane suggests a less rigid polyamide with a smaller degree of cross-linking. This explains its higher water permeability compared to SWC4+. On the other hand, the very low polymer volume fraction of the order of 0.11–0.19 estimated for ESPA1 indicates that its dense core layer may indeed be of the order of 10–20% of what the AFM measures. This yields the spectroscopic thickness  $d_s$  of about 22–40 nm, depending on which IR band was used (Table 3), which is fairly close to what is seen in TEM images (Freger, 2003).

The estimated polymer volume fraction of polyamide was also fairly small for BW30 (Table 3). In this case the reason is apparently the presence of the coating layer rather than the porosity. The spectroscopic thickness of the polyamide layer

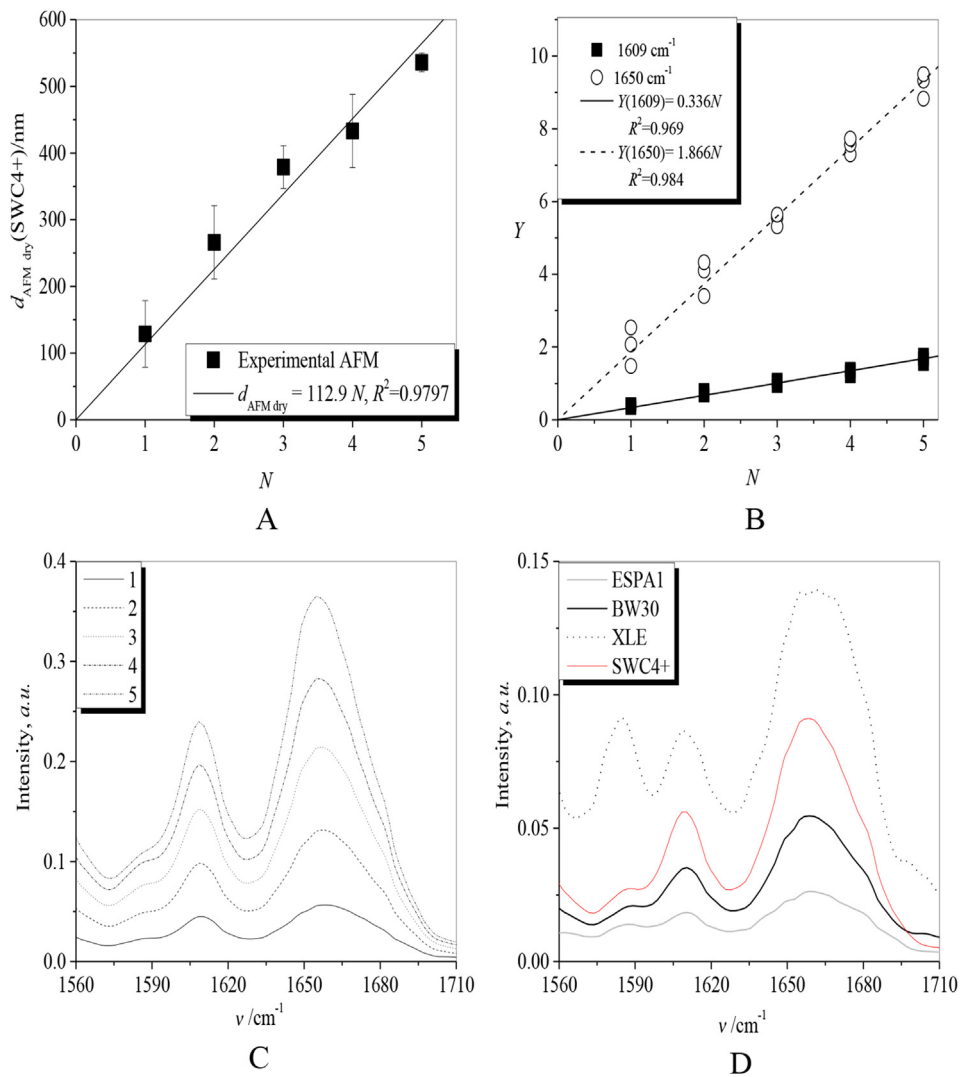


**Fig. 3 – Representative data used for estimating spectroscopic thickness, polymer fraction and porosity of polyamide films. (A) Thicknesses of a stack of polyamide layers measured by AFM versus the number of layers for SWC4+. (B) Areas under the two IR bands, 1609 and 1650  $\text{cm}^{-1}$ , versus number of layers for SWC4+. Integration interval and baselines of IR bands were, 1630 - 1600  $\text{cm}^{-1}$  and 1700-1630  $\text{cm}^{-1}$ , respectively. (C) IR bands at 1609 and 1650  $\text{cm}^{-1}$  of stacked PA films of SWC4+, the legends indicate the number of layers. (D) Same as C for one layer of SWC4+, XLE, ESPA1 and BW30.**

is about 80 nm thick (Table 3), about 2/3 of what AFM measures. Assuming that the thickness measured by AFM is the sum of the thicknesses of the polyamide and coating layers, the polymeric coating layer should be about 40 nm thick.

Again, this estimate fairly closely agrees with the published cross-sectional TEM images of BW30 (Tang et al., 2007).

Even though the spectroscopic thickness may still overestimate the thickness of the truly dense part (the barrier) of

**Table 3 – Calculated polymer volume fractions  $\psi$  and spectroscopic thicknesses  $d_s$  of examined membranes.**

Layer	$d_{AFMdry}/\Delta N$ (AFM)	$\Delta Y/\Delta N$ 1609 (FTIR)	$\Delta Y/\Delta N$ 1650 (FTIR)	$\psi^a$ (1609)	$\psi^a$ (1650)	$d_s^b$ (1609)/nm	$d_s^b$ (1650)/nm
SWC4	112.9	0.336	1.866	1	1	113	113
XLE	188.1	0.399	2.597	0.71	0.82	188	190
ESPA1	214.2	0.068	0.681	0.11	0.19	22 <sup>c</sup>	41 <sup>c</sup>
BW30	125.1	0.163	1.377	0.43	0.65	78 <sup>c</sup>	83 <sup>c</sup>

<sup>a</sup> Polymer volume fraction  $\psi_i = \frac{\Delta Y_i/\Delta N}{\Delta Y_{SWC4+}/\Delta N} \times \frac{d_{AFMdry}(SWC4+)/\Delta N}{d_{dry,i}/\Delta N}$ .

<sup>b</sup> Spectroscopic thicknesses  $d_s(i) = \frac{\Delta Y_i/\Delta N}{\Delta Y_{SWC4+}/\Delta N} \times \frac{d_{AFMdry}(SWC4+)/\Delta N}{\Delta N}$ .

<sup>c</sup> Calculated using assumption that the density of polyamide in ESPA1, BW30 and SWC4+ is identical.

ESPA1 due to the non-negligible contribution by the “fluff”, it may be a more appropriate measure of the thickness than the AFM-based value. The swollen spectroscopic thickness and corresponding intrinsic water permeabilities ( $L_p$  times swollen spectroscopic thickness  $d_s$ ) of this and other membranes are used in the next section to more adequately place each membrane on the water permeability-versus-swelling plot.

### 3.3. Correlation between intrinsic swelling and water permeability

Fig. 4 plots the results as intrinsic permeability versus degree of swelling (water content) for membranes examined in this study along with the previously published data for other membranes and Meares' results for homogeneous films. Meares' results include films of cellulose acetate and polyvinyl alcohol, materials known to show RO or NF performance (Petersen, 1993). The water permeability of each membrane was normalized in two alternative ways by multiplying the measured water permeability  $L_p$  (Table 1) either by the AFM-based swollen thicknesses  $d_{AFM\ wet}$  (Table 2) or the dry ATR-FTIR spectroscopic thickness of PA layers  $d_s$  given in Table 3 divided by  $1 - \phi$  to obtain the swollen spectroscopic thickness. The cellulose acetate films were selected from Meares's data as another material having RO characteristics, i.e., high salt rejection and small intrinsic permeability, and, presumably having “pore radii” commensurate with the polyamide membranes analysed here. Results in Fig. 4 reconfirm that, with the appropriately evaluated thickness and swelling, all the data form a general trend correlating the intrinsic water permeability with water content.

A significant deviation is still observed for ESPA1, even though the use of the spectroscopic thickness brings it much

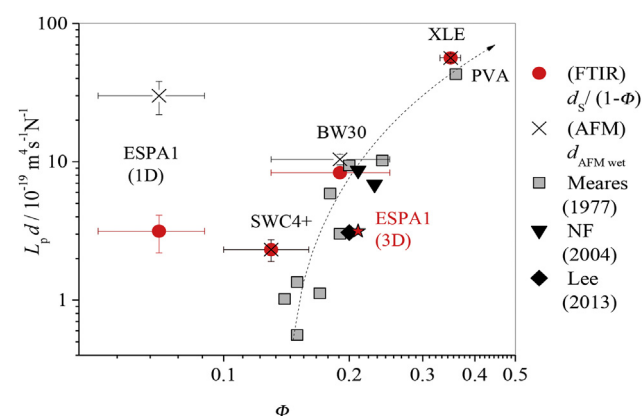


**Fig. 4 – Water permeability plotted versus water content (swelling). The thickness  $d$  in the title of the vertical axis designates either swollen AFM or spectroscopic (FTIR) thickness of measured films, as indicated. Reported data on fully aromatic polyamide RO membrane SW30 (Lee et al., 2013), semiaromatic polyamide NF membranes (Freger, 2004), cellulose acetate films and polyvinyl alcohol (PVA) (Meares, 1977) are shown for comparison. The star designate swelling of ESPA1 evaluated from AFM data assuming 3D expansion; for all other points 1D swelling was assumed. The line is added to guide the eye.**

closer to the trend than in the previous AFM-based estimate (Freger, 2004). The still remaining difference may suggest that either swelling was underestimated or spectroscopic thickness was still an overestimate or both. In either case ESPA1 in Fig. 4 is expected to shift to the right or/and downwards to come closer to the trend. An overestimate of thickness due to the fluffy material is likely, but if the discrepancy is attributed to thickness only, the thickness would have to be unreasonably small, of the order of a nanometre, which would contradict TEM observations (Freger, 2004; Pacheco et al., 2010).

Underestimated swelling is then more likely to be the main reason, even though the present swelling results for ESPA1 are in fair agreement with the previous one (Freger, 2004). It may be assumed that, unlike dense films that are constrained laterally and may expand only in the thickness dimension, the porous “fluff” could expand isotropically into the pores in all 3 dimensions. The same swelling pressure in the fluff part, which makes up most of its superficial (AFM) thickness of ESPA1, may then be achieved at about 1/3 of expansion in each single direction, as compared to one-dimensional expansion of the other membranes. Interestingly, Kurihara presented recently cross-sectional images of a RO membrane, presumably similar to ESPA1, obtained by scanning transmission electron microscopy and elemental maps by electron energy loss spectroscopy indicating that the barrier layer may be significantly folded rather than planar (Kurihara, 2013). In this case the swelling may as well be unconstrained and tri-dimensional thus the vertical expansion sensed by AFM is roughly only 1/3 of the total volume expansion. The relatively small 7% increase in thickness measured by AFM for ESPA1 could then amount to a 3 times larger isotropic volume swelling, i.e., 21% volume fraction of water. Although such a correction is a speculation, Fig. 4 shows that, when this 21% water fraction is combined with spectroscopic thickness of ESPA1 (designated with a star in Fig. 4), it indeed falls reasonable well on the main trend.

Curiously, for BW30 the combination of swelling with overall thickness, both measured by AFM, seems to fall slightly closer to the trend (see Fig. 4) than when the spectroscopic thickness is used. Since the coating fills the defects on the polyamide surface thereby the whole structure (polyamide + coating) is dense, the result may suggest that the trend approximately holds even for such a composite film provided it has no voids. To correctly locate the polyamide layer itself on the trend one needs to have both the correct thickness, for which the spectroscopic thickness may be used, and swelling, which is inaccessible.

Disregarding the above uncertainties for the ESPA1 and BW30, the examined aromatic polyamide membranes seem to follow reasonably well the general trend of water permeability versus swelling previously observed for cellulose acetate and semiaromatic piperazine amide films, as summarized in Fig. 4.

### 3.4. Correlation between intrinsic swelling and selectivity

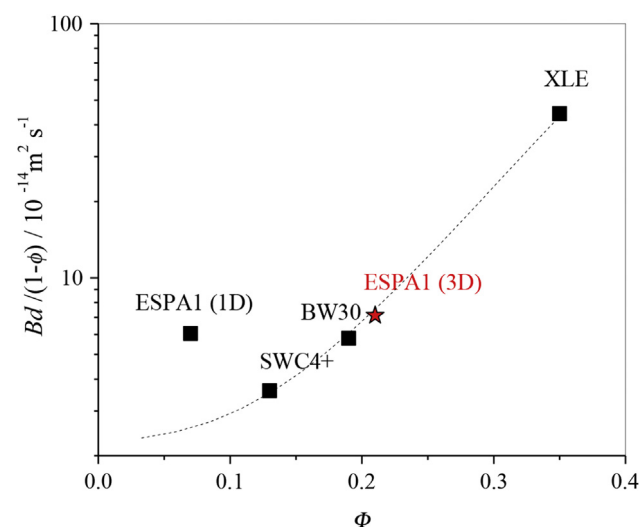
Like the transport of water, the transport of salt and, ultimately, selectivity of the membrane also monotonically varies with the water content. The appropriate material property, analogous to  $L_p d$  in Fig. 4, is the product  $Bd$  of membrane thickness and salt permeability  $B$ . Fig. 5 shows the

dependence of  $Bd$  (based on the wet spectroscopic thickness, i.e.,  $d = d_s/(1 - \phi)$ ) on the water content  $\phi$  for polyamide membranes. To facilitate interpretation, which is more complex than for water permeability (see below), the data points represent only aromatic polyamide. Once again, ESPA1 falls far off the trend when swelling is assumed to be the height expansion measured by AFM (1D), but moves within the trend if its swelling is calculated assuming an isotropic (3D) expansion (the star in Fig. 6). This reinforces the assumption that, opposite to the other thicker membranes, ESPA1 swells isotropically, due to either high porosity, as suggested earlier, or a wiggly non-planar geometry of the active layer, as shown by Kurihara (2013).

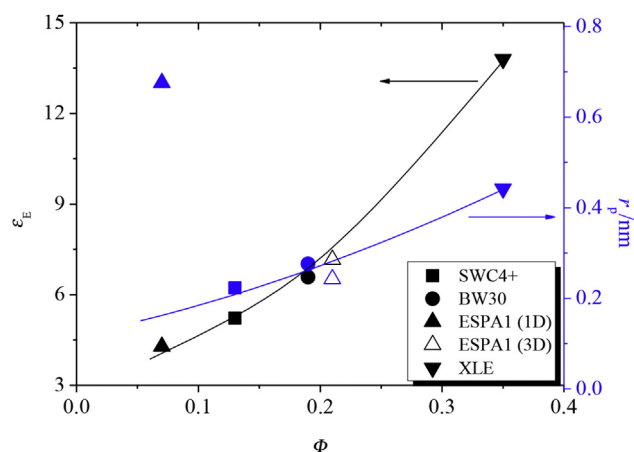
This dependence of  $Bd$  on  $\phi$  may come from several effects. The salt exclusion and permeation in polyamide membranes is believed to be governed by the Donnan, dielectric and steric mechanisms controlled by the fixed charge density, dielectric properties and pore size of the membrane, respectively. Since the fixed charge density is fairly similar for all polyamide membranes (Coronell et al., 2011) and weakly varies with membrane swelling, not much variation of salt permeability with swelling is expected to result from the Donnan exclusion. On the other hand, the average dielectric constant and pore size noticeably increase with water content (see next) and both act to increase the salt permeability. It is then reasonable to assume that, even though the Donnan mechanisms may also play a substantial role in the salt rejection, it is not the dominant factor setting the trend seen in Fig. 5.

Fig. 6 explicitly displays the calculated variation of dielectric constant and pore size with water content. The dielectric constant of the hydrated membrane  $\epsilon_E$  in Fig. 6 was calculated using the Bruggeman equation which is the most adequate model for a random composite (Bruggeman, 1935), as follows

$$\phi \frac{\epsilon_w - \epsilon_E}{\epsilon_w + 2\epsilon_E} + (1 - \phi) \frac{\epsilon_p - \epsilon_E}{\epsilon_p + 2\epsilon_E} = 0, \quad (3)$$



**Fig. 5 – Intrinsic salt permeability plotted versus water content. Intrinsic salt permeability is obtained by multiplying salt permeability,  $B$ , with swollen spectroscopic thickness,  $d_s$  ( $1650 \text{ cm}^{-1}$ )/( $1 - \phi$ ) (Table 3). The line is added to guide the eye.**



**Fig. 6 – Calculated dielectric constant (black symbols),  $\epsilon_E$ , and average pore radii (blue symbols),  $r_p$ , plotted versus water content,  $\phi$ . The dielectric constant was calculated using Eq. (3) and the average pore radius using Eq. (4). The lines are added to guide the eye. (For interpretation of the references to colour in this figure legend, the reader is referred to the web version of this article.)**

where  $\epsilon_p$  (polyamide) = 3.5 and  $\epsilon_w$  (water) = 80. The pore radius,  $r_p$ , was evaluated for each membrane from its  $L_p$  and swollen spectroscopic thickness,  $d_s/(1 - \phi)$  using the following equation,

$$L_p d = \frac{b r_p^2 \phi}{\mu \alpha} \quad (4)$$

where  $r_p$  is the pore radius,  $\mu$  effective viscosity of the solvent,  $\phi$  and  $\alpha$  are the porosity, that can be identified as water content, and tortuosity, respectively. Parameter  $b$  depends on pore geometry and for many random systems  $b = 1/8$  is a reasonable value (Torquato, 2002). Eq. (4) is a generalization of the classic Kozeny–Carman relation, which views random porous medium as a network of connected similarly-sized pores (Torquato, 2002). The calculation of  $r_p$  in Fig. 6 used the relation of tortuosity to porosity  $\alpha(\phi)$  given in Bason et al. (2010) and a constant viscosity of  $\mu = 1 \text{ mPa s}$ .

Dielectric constant appears to be sufficiently low, and vary between 5 and 13 for all membranes, however it must be stressed that the dependence of dielectric exclusion on  $\epsilon_E$  is exponentially strong. Curiously, ESPA1 shows a much smaller  $\epsilon$  and pore radius hence much smaller intrinsic permeability  $Bd$  than XLE, however ESPA1 is much thinner than XLE then both membranes show a similar measured rejection of NaCl, 64%, respectively. Note the measured rejection of salts (64–90%) differs from the manufacturers data (Table 1.) which may be related to lower concentration of the salts used by the manufacturer and to different concentration polarisation due to differences in flow conditions within the commercial elements and the testing cell used here. Concentration polarisation may affect the absolute values of  $B$ , however, it should not change the trend in Fig. 5.

The dielectric effect has already been identified as the mechanism strongly contributing to ion exclusion in RO and NF, both on its own and as a factor enhancing the Donnan

exclusion (Yaroshchuk, 2000; Bandini and Vezzani, 2003; Szymczyk and Fievet, 2005; Bason and Freger, 2010; Bason et al., 2010). It should be noted that dielectric exclusion depends on the pores size and becomes weaker in larger pores (Yaroshchuk, 2000). This pore size-dependence of dielectric exclusion has to be differentiated from the regular size exclusion and may be another factor increasing salt permeability with water content. Nevertheless, the pore radius of all membrane in Fig. 6 is not far from the radii of  $\text{Na}^+$  and  $\text{Cl}^-$  (0.1–0.2 nm depending on the type of ion radius) then the size exclusion may be substantial as well and contribute to variations observed in Fig. 5.

### 3.5. Permeability-swelling correlation: interpretation and relation to selectivity

The general trends observed in Fig. 4 may be rationalized using the standard view on the hydraulic permeability of composite media. As pointed out previously (Freger, 2004; Freger et al., 2000, 1997; Meares, 1977), in most polymer-solvent systems the solvent should have a much higher mobility than polymeric segments. Therefore, in terms of solvent permeability such system may be viewed as random porous media. Then Eq. (4) should generally hold for intrinsic hydraulic permeability of random porous media.

When  $\phi$ , identified here with water content, increases,  $r_p$  increases and  $\alpha$  decreases in a correlated monotonic manner, thereby permeability is correlated with  $\phi$ . Given similar dimensions of polymer chains for many classes of polymers, the scale of  $r_p$  may be fairly similar (cf. Fig. 6) hence the correlation may hold provided effective viscosity  $\mu$  do not vary significantly. This may indeed realistically hold for the polymers considered here, as argued below.

The effective viscosity of water may change at the molecular scale due to enhanced interaction between water molecules within polymer resulting in enhanced clustering. The size of water clusters is mainly related to the chemical nature of the polymer and not as much to water content (Vieth et al., 1969). Remarkably, back in 1977 Strathmann and Michaels observed that in polymers having high salt rejection water molecules do not cluster significantly (Strathmann and Michaels, 1977). In aromatic polyamide and cellulose acetate the clusters were only 2–3 water molecules large. It is then likely that, at the molecular level, individual water molecules in such materials do not interact excessively and do not experience friction with other water molecules much beyond what they do in bulk water. This means the viscosity  $\mu$  in Eq. (4) may indeed stay nearly constant down to molecular scale. This might be part of the reason why the permeability-swelling correlation follows a “universal” correlation for all salt-rejecting films considered here.

With regard to selectivity, the common feature of all examined materials is their high rigidity, achieved through high crosslinking in polyamide or strong chain packing in cellulose acetate or polyvinyl alcohol. It may be postulated that the high rigidity may be a crucial feature of RO membranes, preventing excessive clustering and swelling, as well as formation of a connected network of pores or voids largely exceeding molecular dimensions. The large number of O and N atoms in polyamides, cellulose structure and polyvinyl

alcohol provide multiple hydrogen-bonding sites for water uptake and transport, yet high rigidity ensures that each site binds only very few molecules (cf. clusters of 2–3 molecules found by Stratmann and Michaels). The combination of multiple hydrogen-bonding sites and low water content hence low dielectric properties then allows a reasonable water transport and an efficient dielectric exclusion that keeps the ion transport to minimum. In additions to the low dielectric constant, the pore-size-dependent nature of the dielectric exclusion (see Section 3.4) further dictates that it will operate more efficiently in a dense matrix or in narrow pores than in large water-filled pores. In this way the mechanism of selectivity requiring low swelling, molecularly small pores and weak clustering for good salt rejection might be linked to the trends in Figs. 4 and 5 and explain the superior RO performance of the polymers considered here.

---

## 4. Conclusion

This study has re-examined the relation of water permeability versus water content of thin polymeric films used in RO membranes using more membrane types and improved estimates of thickness and swelling, compared to previous studies. It has shown that combination of AFM as a method to measure swelling and ATR-FTIR for thickness produces more consistent estimates than AFM-based measurements alone, though it still remains challenging to accurately estimate the actual swelling of the polyamide dense core in the highly non-uniform ESPA1 membrane and in the coated BW30 membrane.

Nevertheless, data presented in this study encompassing the most common membrane materials (aromatic polyamide, polypiperazine amide, polyvinyl alcohol, and cellulose acetate) used in RO and NF reconfirm a single general trend connecting intrinsic water permeability and selectivity to swelling (water content) of these materials. The results reported here could add to understanding of the way RO membranes function and be useful in design of new polymeric materials with high salt rejection and good water permeability.

The observed general trend may be rationalized by viewing the polymer as a random porous medium. The crucial common features of polymers showing high salt rejection could be a high rigidity that helps prevent excessive swelling and formation of wide non-selective nanochannels or nanopores, and the presence of multiple hydrogen-bonding sites (O and N atoms) that facilitates transport of water.

---

## Acknowledgement

This project was supported by Croatian Science Foundation through project “Measuring of partitioning of organic solutes between polysulphone/polyamide films and water” and by the Croatian Ministry of Science, Education and Sports through Project 125-1253008-3009 “Membrane and adsorption processes for removal of organic compounds in water treatment”. V. Freger acknowledges the financial support by Israel Science Foundation through grant 1152/11.

## REFERENCES

- Bandini, S., Vezzani, D., 2003. Nanofiltration modelling: the role of dielectric exclusion in membrane characterization. *Chem. Eng. Sci.* 58, 3303.
- Bason, S., Freger, V., 2010. Phenomenological analysis of transport of mono- and divalent ions in nanofiltration. *J. Membr. Sci.* 360, 389.
- Bason, S., Kaufman, Y., Freger, V., 2010. Analysis of ion transport in nanofiltration using phenomenological coefficients and structural characteristics. *J. Phys. Chem. B* 114 (10), 3510–3517.
- Bruggeman, D.A.G., 1935. Berechnung verschiedener physikalischer Konstanten von heterogenen Substanzen. I. Dielektrizitätskonstanten und Leitfähigkeiten der Mischkörper aus isotropen Substanzen. *Annalen der Physik* 416 (7), 636–664.
- Coronell, O., Mariñas, B.J., Cahill, D.G., 2011. Depth heterogeneity of fully aromatic polyamide active layers in reverse osmosis and nanofiltration membranes. *Environ. Sci. Technol.* 45 (10), 4513–4520.
- Dražević, E., Bason, S., Košutić, K., Freger, V., 2012. Enhanced partitioning and transport of phenolic micropollutants within polyamide composite membranes. *Environ. Sci. Technol.* 46 (6), 3377–3383.
- Freger, V., 2003. Nanoscale heterogeneity of polyamide membranes formed by interfacial polymerization. *Langmuir* 19, 4791–4797.
- Freger, V., 2004. Swelling and morphology of the skin layer of polyamide composite membranes. *Environ. Sci. Technol.* 38, 3168.
- Freger, V., Korin, E., Wisniak, J., Korngold, E., 2000. Measurement of sorption in hydrophilic pervaporation: sorption modes and consistency of the data. *J. Membr. Sci.* 164 (1–2), 251–256.
- Freger, V., Korin, E., Wisniak, J., Korngold, E., 1997. Transport mechanism in ion-exchange pervaporation membranes: dehydration of water–ethanol mixture by sodium polyethylene sulphonate membranes. *J. Membr. Sci.* 133, 255.
- Kim, S.H., Kwak, S.-Y., Suzuki, T., 2005. Positron annihilation spectroscopic evidence to demonstrate the flux-enhancement mechanism in morphology-controlled thin-film-composite (TFC) membrane. *Environ. Sci. Technol.* 39 (6), 1764–1770.
- Košutić, K., Kaštelan-Kunst, L., Kunst, B., 2000. Porosity of some commercial reverse osmosis and nanofiltration polyamide thinfilm composite membranes. *J. Membr. Sci.* 168, 101–108.
- Kurihara, M., 2013. Membrane research for water treatment facing the age of global mega-competition and collaboration. In: *Advances in Materials and Processes for Polymeric Membrane Mediated Water Purification*, Pacific Grove, CA.
- Lee, J., Doherty, C.M., Hill, A.J., Kentish, S.E., 2013. Water vapor sorption and free volume in the aromatic polyamide layer of reverse osmosis membranes. *J. Membr. Sci.* 425–426, 217–226.
- Meares, P., 1977. The mechanism of water transport in membranes. *Phil. Trans. R.Soc. Lon. B* 270, 113–150.
- Meares, P., 1976. In: Meares, P. (Ed.), *Membrane Separation Processes*. Elsevier, Amsterdam.
- Pacheco, C.A., Pinnau, I., Reinhard, M., Leckie, J.O., 2010. Characterization of isolated polyamide thin films of RO and NF membranes using novel TEM techniques. *J. Membr. Sci.* 358, 51.
- Petersen, R.J., 1993. Composite reverse osmosis and nanofiltration membranes. *J. Membr. Sci.* 83, 81.
- Strathmann, H., Michaels, A.S., 1977. Polymer-water interaction and its relation to reverse osmosis desalination efficiency. *Desalination* 21, 195–202.
- Szymczyk, A., Fievet, P., 2005. Investigating transport properties of nanofiltration membranes by means of a steric, electric and dielectric exclusion model. *J. Membr. Sci.* 252, 77.
- Tang, C.Y., Kwon, Y.-N., Leckie, J.O., 2009. Effect of membrane chemistry and coating layer on physiochemical properties of thin film composite polyamide RO and NF membranes I. FTIR and XPS characterization of polyamide and coating layer chemistry. *Desalination* 242, 149–167.
- Tang, C.Y., Kwon, Y.-N., Leckie, J.O., 2007. Probing the nano- and micro-scales of reverse osmosis membranes—a comprehensive characterization of physiochemical properties of uncoated and coated membranes by XPS, TEM, ATR-FTIR, and streaming potential measurements. *J. Membr. Sci.* 287, 146–156.
- Tarleton, E.S., Robinson, J.P., Salman, M., 2006. Solvent-induced swelling of membranes — measurements and influence in nanofiltration. *J. Membr. Sci.* 280, 442–451.
- Torquato, S., 2002. *Random Heterogeneous Materials: Microstructure and Macroscopic Properties*. Springer-Verlag, New York.
- Vieth, W., Douglas, A.S., Bloch, R., 1969. Membrane-water structural interactions in reverse osmosis transport. *J. Macromol. Sci.-Phys. B* 4, 737–749.
- Yaroshchuk, A.E., 2000. Dielectric exclusion of ions from membranes. *Adv. Colloid Interf. Sci.* 85, 193.